

# Pressure Support vs. Thermal Broadening in the Lyman- $\alpha$ Forest II: Effects of the Equation of State on Transverse Structure

Molly S. Peeples<sup>1\*</sup>, David H. Weinberg<sup>1</sup>, Romeel Davé<sup>2</sup>, Mark A. Fardal<sup>3</sup>, Neal Katz<sup>3</sup>

<sup>1</sup>*Department of Astronomy and the Center for Cosmology and Astro-Particle Physics, The Ohio State University, Columbus, OH 43210*

<sup>2</sup>*University of Arizona, Steward Observatory, Tucson, AZ 85721*

<sup>3</sup>*Department of Astronomy, University of Massachusetts, Amherst, MA 01003*

17 November 2018

## ABSTRACT

We examine the impact of gas pressure on the transverse coherence of high-redshift ( $2 \leq z \leq 4$ ) Lyman- $\alpha$  forest absorption along neighboring lines of sight that probe the gas Jeans scale (projected separation  $\Delta r_p \leq 500 h^{-1}$  kpc comoving; angular separation  $\Delta\theta \lesssim 30''$ ). We compare predictions from two smoothed particle hydrodynamics (SPH) simulations that have different photoionization heating rates and thus different temperature-density relations in the intergalactic medium (IGM). We also compare spectra computed from the gas distributions to those computed from the pressureless dark matter. The coherence along neighboring sightlines is markedly higher for the hotter, higher pressure simulation, and lower for the dark matter spectra. We quantify this coherence using the flux cross-correlation function and the conditional distribution of flux decrements as a function of transverse and line-of-sight (velocity) separation. Sightlines separated by  $\Delta\theta \lesssim 15''$  are ideal for probing this transverse coherence. Higher pressure decreases the redshift-space anisotropy of the flux correlation function, while higher thermal broadening increases the anisotropy. In contrast to the longitudinal (line-of-sight) structure of the Ly $\alpha$  forest, the transverse structure on these scales is dominated by pressure effects rather than thermal broadening. With the rapid recent growth in the number of known close quasar pairs, paired line-of-sight observations offer a promising new route to probe the IGM temperature-density relation and test the unexpectedly high temperatures that have been inferred from single sightline analyses.

**Key words:** cosmology: miscellaneous — intergalactic medium — methods: numerical

## 1 INTRODUCTION

The  $1.5 \lesssim z \lesssim 6$  intergalactic medium (IGM) is most commonly studied via the Lyman- $\alpha$  forest, which arises from Ly $\alpha$  absorption of neutral hydrogen along the line of sight to some distant source (e.g., a quasar). Most of the information we have on the nature of the IGM is from sightlines piercing physically distinct regions of the IGM. Absorption features have finite widths, but from individual sightlines it is difficult to separate the contribution of bulk velocities (Hubble flow and peculiar velocities) from those of thermal broadening. Close quasar pairs can break this degeneracy by probing the transverse structure of the IGM. In the mid-1990s, several studies of quasar groups and lensed quasars definitively showed that the absorbing structures are coherent over hundreds of kpc (Bechtold et al. 1994; Dinshaw et al. 1994; Fang et al. 1996; Charlton et al. 1997; Crofts & Fang 1998; D’Odorico et al. 1998). These observations provided critical support for the physical picture of the Ly $\alpha$  forest then emerging from cosmological simulations (Cen et al. 1994; Zhang et al.

1995; Hernquist et al. 1996) and associated analytic descriptions (Rauch & Haehnelt 1995; Reisenegger & Miralda-Escudé 1995; Bi & Davidsen 1997; Hui et al. 1997), in which most Ly $\alpha$  absorption arises in a continuously fluctuating medium of low density gas rather than in a system of discrete clouds. More recently, observations of pairs have been suggested as ways of investigating measuring the cosmological constant via the Alcock & Paczynski (1979) effect (McDonald & Miralda-Escudé 1999), the matter power spectrum on small scales (Viel et al. 2002), and the IGM temperature-density relation. It is on the last of these that we focus in this paper.

Theoretical models predict that the low density IGM should have a power-law “equation of state,”

$$T = T_0(1 + \delta)^\alpha, \quad (1)$$

with denser gas being hotter than less dense gas ( $\alpha > 0$ , Katz et al. 1996; Miralda-Escudé et al. 1996; Hui & Gnedin 1997). Although this temperature-density ( $T$ - $\rho$ ) relation is difficult to measure, multiple observations suggest that it has a higher normalization and a shallower slope than that expected using the most straightforward assumptions about photoionization heating (Schaye et al. 2000; McDonald et al. 2001; Theuns et al. 2002; Bolton et al. 2008). Be-

\* E-mail: molly@astronomy.ohio-state.edu

cause the degree of small-scale transverse coherence is set by the Jeans length, and the Jeans length depends on the temperature of the gas, studying the transverse structure of the Ly $\alpha$  forest might give insight into the IGM  $T$ - $\rho$  relation (J. Hennawi, private communication, 2007). In Peeples et al. (2009, hereafter Paper I), we show that while thermal broadening and pressure support both affect the longitudinal structure of the Ly $\alpha$  forest, thermal broadening dominates. In this paper we investigate the effects of the temperature-density relation via pressure support and thermal broadening on the transverse small-scale structure of the Ly $\alpha$  forest.

The gas temperature affects the Jeans length  $\lambda_J$  (and the comoving Jeans length  $\lambda_{J,\text{comv}}$ ) via

$$\lambda_J \equiv c_s \sqrt{\frac{\pi}{G\rho}} \quad (2)$$

$$\begin{aligned} \Rightarrow \lambda_{J,\text{comv}} &= (1+z)\sigma_{\text{th}}H_0^{-1} \sqrt{\frac{5\pi}{3}} \left[ \frac{3}{8\pi}\Omega_{m,0}(1+z)^3(1+\delta) \right]^{-1/2} \\ &= 782 h^{-1} \text{ kpc} \\ &\times \left( \frac{\sigma_{\text{th}}}{11.8 \text{ km s}^{-1}} \right) \left[ \left( \frac{\Omega_{m,0}(1+\delta)}{0.25 \times (1+0)} \right) \left( \frac{1+z}{1+3} \right) \right]^{-1/2}, \end{aligned} \quad (3)$$

where  $1+\delta \equiv \rho_{\text{gas}}/\bar{\rho}_b$  is the gas overdensity and  $c_s = \sqrt{[5kT]/[3m]} = \sigma_{\text{th}}\sqrt{5/3}$  is the speed of sound in an ideal gas expressed as a multiple of the 1-D thermal velocity  $\sigma_{\text{th}}$ , which we have normalized to correspond to  $10^4$  K (Miralda-Escudé et al. 1996; Schaye 2001; Desjacques & Nusser 2005). While thermal broadening affects the observed IGM by smoothing the Ly $\alpha$  forest in one-dimension (namely, along the line of sight), pressure support smooths the physical gas distribution in all three dimensions. Therefore, while we found in Paper I that  $\sigma_{\text{th}}$  dominates the longitudinal Ly $\alpha$  forest structure, we expect  $\lambda_J$  to dominate the transverse structure. Our simulations indicate that the “effective” Jeans length in the Ly $\alpha$  forest is smaller than that given in Equation (3) by a factor of a few, probably owing to a combination of geometric factors, the universe expanding on the same timescale as the gas evolves, and the contribution of dark matter to the gravitational forces (see also Gnedin & Hui 1998).

For  $\Omega_m = 0.25$  and  $\Omega_\Lambda = 0.75$ , the relation between angular separation  $\Delta\theta$  and comoving transverse separation  $R$  at  $z = 2-4$  is approximately

$$\Delta\theta \approx 4.4'' \left( \frac{1+z}{4} \right)^{0.6} \times \left( \frac{R}{100 h^{-1} \text{ kpc}} \right). \quad (4)$$

Lines of sight with angular separations of  $3-10''$  are needed to probe the Jeans scale of the IGM. While this scale is just larger than the cutoff for the typical Einstein radius of galaxy lenses (Schneider, Kochanek, & Wambsganss 2006), new searches for binary quasars are revealing samples of a few to dozens with  $\Delta\theta \lesssim 10''$  (Hennawi et al. 2006, 2009).

This paper is organized as follows. In § 2, we describe the SPH simulations used, as well as the artificial temperature-density relations we impose on the gas to isolate the effects of pressure support and thermal broadening. In § 3 we discuss how the temperature-density relation affects the transverse coherence of the Ly $\alpha$  forest, with particular focus on flux cross-correlation functions and conditional flux probability distributions. We find that, as expected, the transverse coherence of the Ly $\alpha$  forest across closely paired sight-lines is dominated by the amount of pressure support in the absorbing gas. These conclusions are summarized in § 4. In an Appendix and associated electronic tables, we provide Ly $\alpha$  forest spectra extracted from our simulations at several transverse separations that can be used to create predictions tailored to specific observational

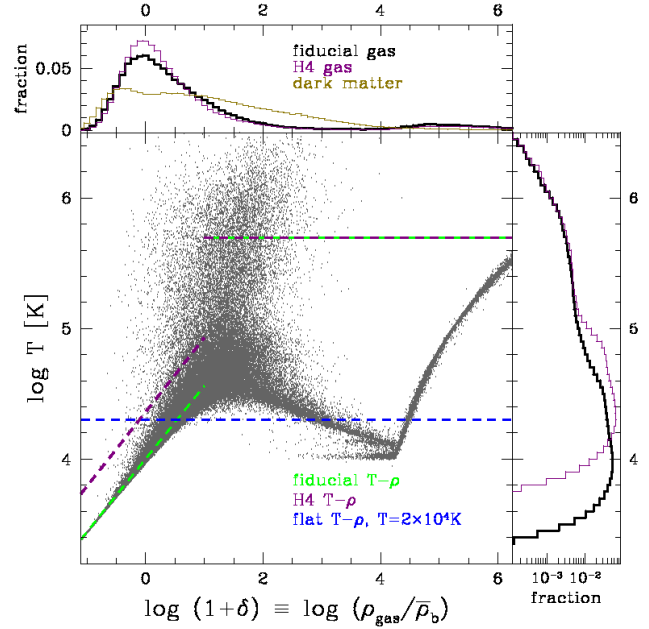


**Figure 1.** Distribution of particles in the temperature-overdensity plane for the fiducial simulation at  $z = 2.4$ , with three imposed temperature-density relations over-plotted as labelled, as well as the temperature and overdensity distributions for the fiducial and H4 simulations. The hotter H4 gas is preferentially less dense than the lower pressure fiducial gas and pressure-less dark matter.

analyses. We note that Paper I includes an extensive discussion of the physical structure of the Ly $\alpha$  forest in these simulations, so in this paper we will focus only on those issues relevant to quasar pair observations. All distances are given in comoving coordinates unless otherwise stated.

## 2 SIMULATIONS

We use the same  $2 \times 288^3$  particle  $12.5 h^{-1} \text{ Mpc}$  comoving smoothed particle hydrodynamic (SPH) simulations evolved with GADGET-2 (Springel 2005) as in Paper I; hence we only present a basic description here. Throughout we adopt a  $\Lambda$ CDM cosmology of  $(\Omega_m, \Omega_\Lambda, \Omega_b, h, \sigma_8, n_s) = (0.25, 0.75, 0.044, 0.7, 0.8, 0.95)$ , which is in good agreement with the *Wilkinson Microwave Anisotropy Probe* 5-year results (Hinshaw et al. 2009). This cosmology leads to a gas particle mass of  $1.426 \times 10^6 M_\odot$ , which is much less than the expected typical Jeans mass of  $\sim 7 \times 10^9 M_\odot$ . As a convergence test, we use a  $2 \times 144^3$  particle simulation that is otherwise identical to our fiducial simulation. The distribution of particles in the temperature-density plane for our “fiducial” simulation at  $z = 3$  is shown in Figure 1. The “H4” simulation has the same initial conditions as the fiducial one, but the heating rate from photoionization by the UV background is four times higher than in the fiducial simulation. An obvious consequence of this higher heating rate is that the H4 gas has higher temperatures than the fiducial gas. A more subtle effect, also shown in Figure 1, is that the hotter gas has a larger Jeans length and is hence smoother, with a smaller fraction of the gas at high overdensity. We therefore adopt three artificial temperature-density relations to isolate the effects of pressure support, thermal broadening, and the underlying overdensity distribution. As in Paper I, the fiducial and H4

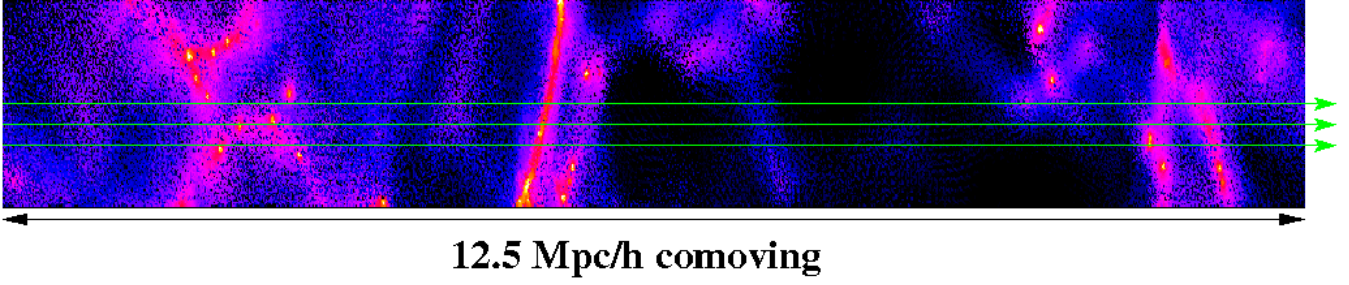


**Figure 2.** A  $12.5 \times 1 \times 1 h^{-1}$  Mpc comoving section of the fiducial simulation, in H I density, with  $-8 < \log n_{\text{HI}} < 0$  (note that the aspect ratio has not been preserved). The three green sightlines are separated by  $100 h^{-1}$  kpc comoving; at  $z = 2.4$ , corresponding to a projected separation of  $4.9''$ .

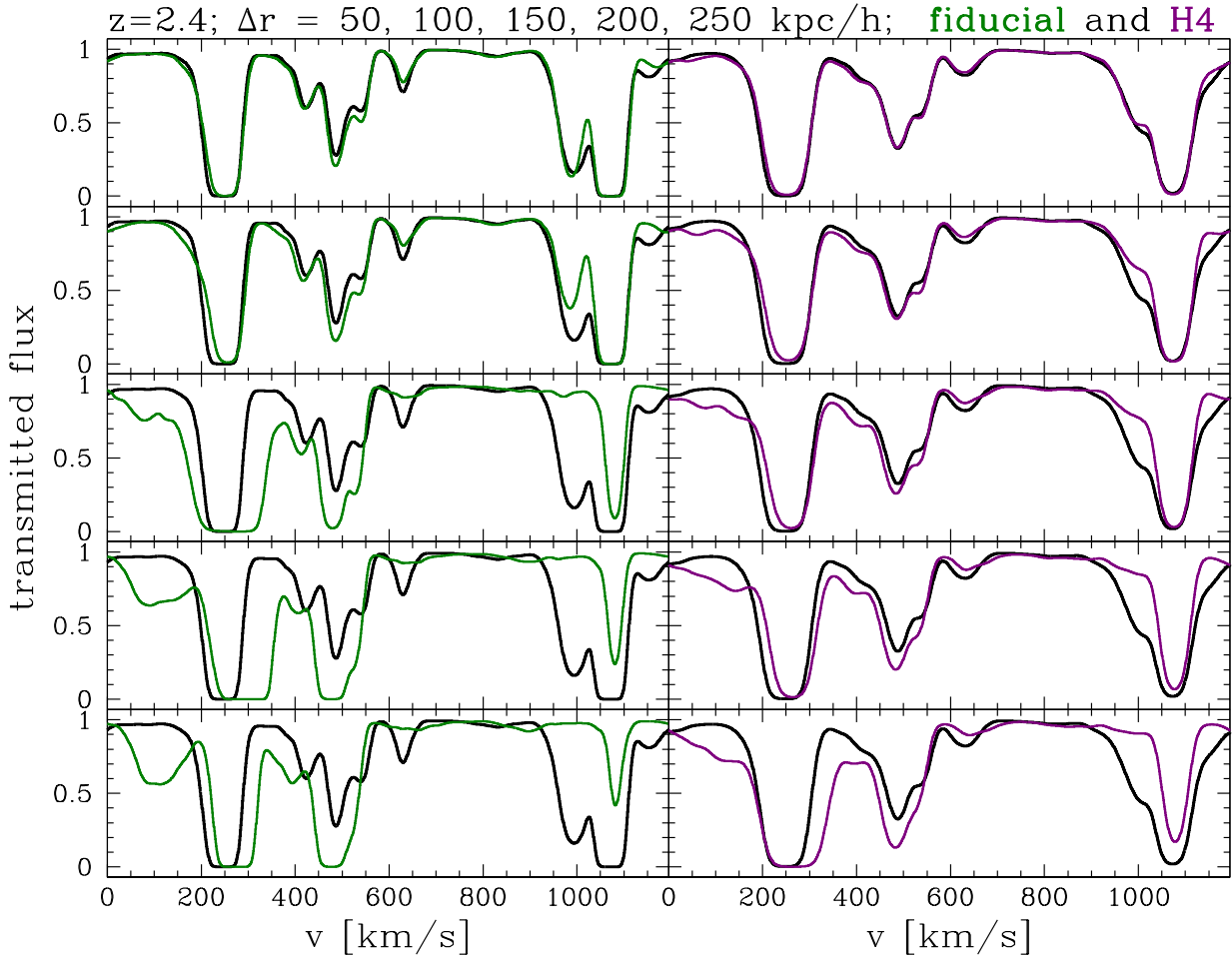


**Figure 3.** Sample paired lines of sight at  $z = 2.4$  separated by  $\Delta r = 50, 100, 150, 200$ , and  $250 h^{-1}$  kpc comoving, from top to bottom, with the fiducial simulation on the left and the H4 simulation on the right. Within each column, the black spectra are the same ( $r = 0$ ). The top, middle, and bottom green spectra correspond to the three green sightlines in Fig. 2, with  $v = 0$  corresponding to the left-hand side of Fig. 2.

temperature-density relations mimic the ones found in those simulations, while the flat  $T = 2 \times 10^4$  K relation is used so that we can study the effects of thermally-broadened pressure support in the absence of overdensity-dependent thermal broadening. We impose these temperature-density relations on the fiducial and H4 gas distributions, as well as the fiducial dark matter, by assigning temperatures based solely on the local gas (or dark matter) overdensity, as demonstrated in Figure 1. For the fiducial and H4 relations, we set all gas with  $1 + \delta \geq 10$  to a “shocked” temperature  $T = 5 \times 10^5$  K,

while for the flat relation we set all the gas to  $T = 2 \times 10^4$  K, regardless of density.

At each redshift— $z = 2, 2.4, 3$ , and  $4$ —we consider 200 lines of sight with paired sightlines separated by  $\Delta r = 50, 100, 125, 150, 175, 200, 250, 300, 400$ , and  $500 h^{-1}$  kpc comoving for a total of 2200 sightlines per redshift for each of the overdensity- $T$ - $\rho$  combinations discussed above. In all cases we adjust the intensity of the UV background so that the mean flux decrement matches observational estimates (see Paper I for details). In Table 1, we list the

**Table 1.** Observed mean flux decrements  $\langle D \rangle \equiv \langle 1 - e^{-\tau} \rangle$  at  $z = 2.4, 3$ , and 4 are from McDonald et al. (2000); the  $z = 2$  measurement is from Faucher-Giguère et al. (2008) without correcting for metal absorption. The observed temperature-density relations ( $T = T_0[1 + \delta]^\alpha$ ) at  $z = 2.4, 3$ , and 4 are from McDonald et al. (2001), with the  $z \sim 2$  measurement from Ricotti et al. (2000).

$z$	$\langle D \rangle$	observed $T_0$ [K]	observed $\alpha$	fiducial $T_0$ [K]	fiducial $\alpha$	H4 $T_0$ [K]	H4 $\alpha$	$\Delta\theta$ at $100 h^{-1}$ kpc
4.0	$0.525 \pm 0.012$	$17400 \pm 3900$	$0.43 \pm 0.45$	11700	0.54	28200	0.55	$3.9''$
3.0	$0.316 \pm 0.023$	$18300 \pm 1800$ or $18400 \pm 2100$	$0.33 \pm 0.26$ $0.29 \pm 0.30$	11000	0.57	25000	0.57	$4.4''$
2.4	$0.182 \pm 0.021$	$17400 \pm 1900$ or $19200 \pm 2000$	$0.52 \pm 0.14$ $0.51 \pm 0.14$	10000	0.56	23000	0.57	$4.9''$
2.0	$0.144 \pm 0.024$	17700	$0.32 \pm 0.30$	8913	0.56	21380	0.57	$5.4''$

adopted mean decrements and parameters for the observed, fiducial, and H4 temperature-density relations, as well as the projected angular separation at  $100 h^{-1}$  kpc comoving.

### 3 STRUCTURE OF THE IGM & TRANSVERSE $\text{Ly}\alpha$ COHERENCE

To gain insight into the effects of temperature on the transverse coherence of the  $\text{Ly}\alpha$  forest, we look at how paired sightlines differ in the fiducial and H4 simulations in § 3.1. We then quantify these differences by examining the relative changes in the flux decrement cross-correlation function in § 3.2 and the relative transverse coherence of the conditional flux decrement probability distribution in § 3.3.

#### 3.1 Spectra

Before delving into statistical measures of the transverse  $\text{Ly}\alpha$  forest, it will be instructive to first consider the underlying physical structures. In Figure 2, we show a small section of the fiducial simulation at  $z = 2.4$ , where brighter regions correspond to higher H I densities. The observed transmitted flux is calculated as simply

$$F = e^{-\tau_{\text{Ly}\alpha}}, \quad (5)$$

where  $\tau_{\text{Ly}\alpha}$  is the optical depth to  $\text{Ly}\alpha$  photons. As discussed in detail in Paper I,

$$\begin{aligned} \tau_{\text{Ly}\alpha} &\propto n_{\text{HI}} \\ &\propto \left( \frac{T_0}{10^4 \text{ K}} \right)^{-0.7} (1 + \delta)^{2-0.7\alpha}. \end{aligned} \quad (6)$$

The three sightlines in Figure 2 give rise to the top, middle, and bottom green spectra at  $z = 2.4$  in the left-hand panel of Figure 3. Figure 3 shows how pairs of spectra become more dissimilar as their transverse separation,  $\Delta r$ , increases, and how this dissimilarity differs between the fiducial and H4 simulations. Spectral features remaining coherent over large scales correspond to physical structures that are parallel to the plane of the sky (see, e.g., the structures at  $400 < v < 600 \text{ km s}^{-1}$ ), while spectral features disappearing from one sightline to the next correspond to physical structures that are more parallel to the line of sight (see, e.g., the features at  $v < 300 \text{ km s}^{-1}$ ). In general, the H4 spectra remain more similar than the fiducial ones as  $\Delta r$  increases; we aim to determine to what extent this relatively higher coherence owes to pressure support rather than to the fact that the H4 spectra are individually

inherently smoother because they have more thermal broadening than the fiducial spectra.

#### 3.2 Cross-Correlation Functions

A common method for studying the transverse structure of the IGM is to look at the flux decrement cross-correlation function,

$$\xi_{\text{cross}} \equiv \frac{\langle D_1(v) D_2(v + \Delta v) \rangle}{\langle D \rangle^2}, \quad (7)$$

where  $D \equiv 1 - F = 1 - \exp(-\tau)$  and the two sightlines are separated by some  $\Delta r$  (Miralda-Escudé et al. 1996; Rollinde et al. 2003). At  $\Delta r = 0$ ,  $\xi_{\text{cross}}$  is just the auto-correlation function. The cross-correlation functions for the  $z = 2.4$  fiducial and H4 simulations at a range of  $\Delta r$  are shown in the left-hand panels of Figure 4. At small  $\Delta r$  and  $\Delta v$ , the gas in the fiducial simulation has a higher  $\xi_{\text{cross}}$  than the gas in the H4 simulation because the smoother gas distribution has less rms density fluctuation. At larger  $\Delta r$  and  $\Delta v$ , the H4 gas has a higher  $\xi_{\text{cross}}$  owing to its greater coherence, as is visually evident in Figure 3. To quantify this relative change,  $\xi_{\text{cross}}/\xi_{\text{auto}}$  for the same selection of  $\Delta r$  is plotted in the right-hand panels of Figure 4. Although in real space  $\xi_{\text{cross}}(\Delta r) = \xi_{\text{auto}}(H\Delta r)$ , in velocity space redshift distortions preferentially suppress the auto-correlation function relative to the cross-correlation function, causing  $\xi_{\text{cross}} > \xi_{\text{auto}}$  for some regions of parameter space (McDonald & Miralda-Escudé 1999; Marble et al. 2008b). The hotter, higher pressure, H4 simulation has a higher relative coherence (larger  $\xi_{\text{cross}}/\xi_{\text{auto}}$ ) at small  $\Delta v$  than the colder fiducial simulation.

We compare a wider range of models in Figure 5, where we plot  $\xi_{\text{cross}}/\xi_{\text{auto}}$  as a function of  $\Delta r$  at  $\Delta v = 20 \text{ km s}^{-1}$  at  $z = 2.4$ ; this corresponds to taking a slice at  $\Delta v = 20 \text{ km s}^{-1}$  in the right-hand panels of Figure 4. To elucidate whether the H4 gas is more strongly correlated because it has higher pressure, or because, as shown in detail in Paper I, hotter gas has more thermal broadening and therefore less small-scale structure, we also look at a range of  $T$ - $\rho$  relations and overdensity fields. In this and in several of the following figures the line type (solid, dashed, or dotted) corresponds to the adopted overdensity field, either the gas overdensities from the fiducial simulation (solid lines), the gas overdensities from the H4 simulation (dashed lines) or the dark matter overdensities from the fiducial simulations. The line color corresponds to the adopted equation of state, i.e. the  $T$ - $\rho$  relation, either the artificial fit to the relation from the fiducial simulation (green lines), the fit to the relation from the H4 simulation (red lines), or assuming a constant temperature of  $T = 2 \times 10^4 \text{ K}$  (blue lines).



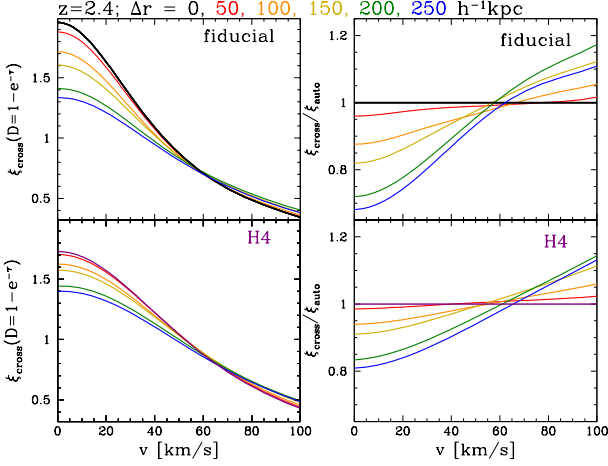


**Figure 4.** The cross-correlation function  $\xi_{\text{cross}} \equiv \langle D_1(v)D_2(v+\Delta v) \rangle / \langle D \rangle^2$  (left) and  $\xi_{\text{cross}}/\xi_{\text{auto}}$  (right) for the fiducial (top) and H4 (bottom) simulations for six different transverse separations  $\Delta r = 50, 100, 150, 200$ , and  $250 h^{-1}$  kpc comoving. Note that the vertical scale in the left panels does not extend to 0.

In Figure 5, the three choices for the overdensity field clearly separate into three distinct groups, with the highest-pressure H4 gas having the most transverse coherence and the zero-pressure dark matter having the least. Even non-thermally broadened spectra (which we have not plotted to avoid visual confusion) show the same relative decrease in coherence with increase in transverse separation as other spectra with the same underlying gas distributions. Within each overdensity group,  $\xi_{\text{cross}}/\xi_{\text{auto}}$  increases with increasing thermal broadening (e.g., the imposed H4  $T$ - $\rho$  relation yields higher  $\xi_{\text{cross}}/\xi_{\text{auto}}$  at all  $\Delta r$  than imposing the fiducial  $T$ - $\rho$ ). However, lowering the resolution leads to offsets from the fiducial case by about the same amount as imposing different  $T$ - $\rho$  relations. The same trends are seen at  $z = 2, 3$ , and  $4$ , as shown in Figure 6. In general, we find this delineation is clearer at  $10 \lesssim \Delta v \lesssim 30 \text{ km s}^{-1}$  than at  $\Delta v = 0$  or at larger velocity separations. The stark separation by overdensity distribution of the normalized cross-correlation function as a function of transverse separation is a clear sign that pressure plays an important role in the transverse structure of the Ly $\alpha$  forest.

A common use for the flux decrement cross-correlation function is to measure the anisotropy in the Ly $\alpha$  forest caused by line-of-sight velocity distortions (Coppolani et al. 2006; D’Odorico et al. 2006), such as for the Alcock & Paczynski (1979) test (Hui et al. 1999; McDonald & Miralda-Escudé 1999). In Figure 7, we compare  $\xi_{\text{cross}}(\Delta v = 0, \Delta r)$  to the autocorrelation function at the same scale,  $\xi_{\text{auto}}(H\Delta r)$ , at  $z = 2.4$ ; higher values indicate higher levels of anisotropy. As in Figure 5, the models separate into groups of overdensity, and the differences between our low-resolution and fiducial cases are comparable with imposing different  $T$ - $\rho$  relations on the fiducial gas. Figure 8 shows the same statistic for a smaller set of models at  $z = 2, 3$ , and  $4$ . As mentioned above, in real space  $\xi_{\text{cross}}(\Delta r) = \xi_{\text{auto}}(H\Delta r)$ , but in (observed) velocity space, redshift distortions introduce anisotropy (Marble et al. 2008b). Because thermal broadening is an inherently one-dimensional anisotropic phenomenon, higher thermal broadening leads to higher anisotropy; we see this effect for each overdensity distribution in Figures 7 and 8. Pressure, on the other hand, is a three-dimensional inherently isotropic phenomenon: higher pressure therefore leads to less anisotropy, as we see from comparing

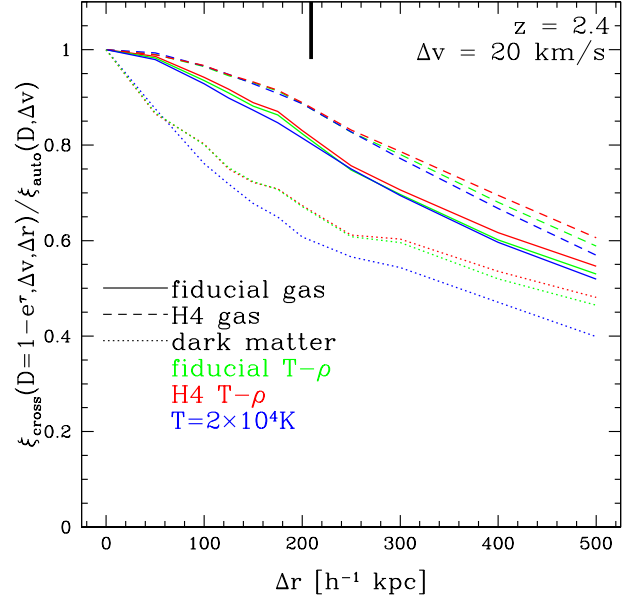


**Figure 5.** Normalized cross-correlation functions,  $\xi_{\text{cross}}/\xi_{\text{auto}}$ , as a function of the transverse separation  $\Delta r$  for  $\Delta v = 20 \text{ km s}^{-1}$  at  $z = 2.4$ . The line type (solid, dashed, or dotted) denotes the adopted overdensity field and the line color the adopted  $T$ - $\rho$  relation (see § 2 for details). The thick black tickmark denotes  $\Delta r = H\Delta v$ .

the results for the dark matter, fiducial, and H4 overdensity fields. For  $H\Delta r \lesssim 20 \text{ km s}^{-1}$  ( $\Delta\theta \lesssim 10''$ ), the impact of thermal broadening on anisotropy is generally smaller than the impact of pressure.

### 3.3 Conditional Flux Probability Distributions

The structure of one-point flux probability distribution function (PDF) depends on both the thermal history and current thermal state of the gas, leading to a complex relationship between the effects of pressure support and thermal broadening on the PDF (Paper I). On the other hand, the interpretation of the conditional probability distribution function between paired sightlines (Miralda-Escudé et al. 1997) is relatively straightforward. For example, if for strongly absorbed pixels with  $0.8 \leq D_1 < 1.0$ , the pixels separated by  $\Delta v$  on a sightline  $\Delta r$  away are more strongly absorbed than randomly expected, then this might be a signature of strong transverse coherence and thus a large Jeans length. In Figure 9 we plot the flux decrement difference probability distributions,  $p(D_2 - D_1)$ , for  $\Delta v = 0$  and  $\Delta r = 150 h^{-1}$  kpc and several bins of  $D_1$ , for the fiducial, H4, and low resolution gas at  $z = 2.4$ . By looking at the PDF of the decrement differences, we can easily quantify the similarity of flux decrement pairs. The more strongly the distribution peaks around  $D_2 = D_1$ , the more coherent are the transverse structures. While the differences between the two simulations are not dramatic, the H4 model is consistently more strongly peaked around  $D_2 = D_1$ , with a stronger signature at low  $D_1$ . For most choices of  $D_1$ , this difference is much more pronounced than the difference between the fiducial and low-resolution simulations, indicating that our  $288^3$  particle simulations give robust results for this statistic.

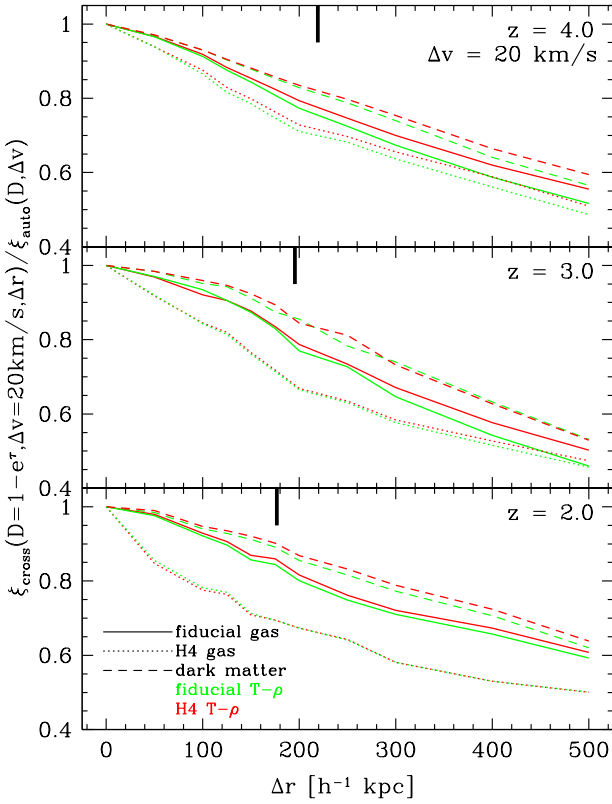


**Figure 6.** Normalized cross-correlation functions,  $\xi_{\text{cross}}/\xi_{\text{auto}}$ , as a function of the transverse separation  $\Delta r$  for  $\Delta v = 20 \text{ km s}^{-1}$  at  $z = 4, 3$ , and  $2$ , from top to bottom. The models are denoted as in Fig. 5. The thick black tickmark denotes  $\Delta r = H\Delta v$ .

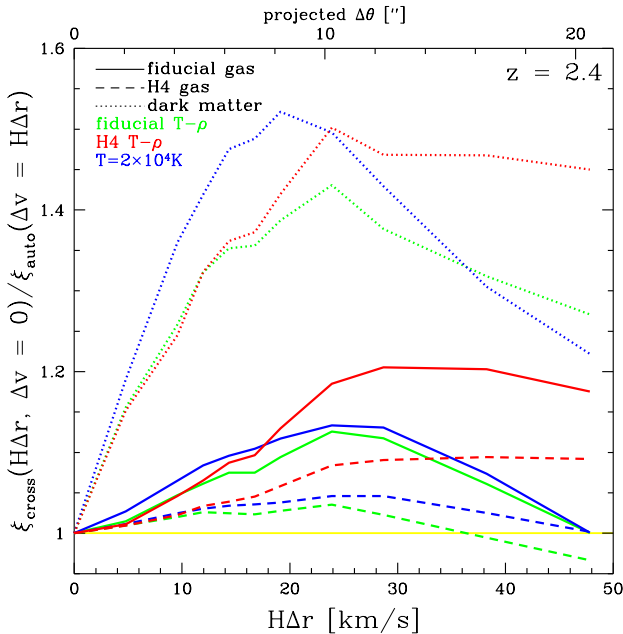


**Figure 7.** Normalized cross-correlation functions showing the anisotropy of the Ly $\alpha$  forest,  $\xi_{\text{cross}}/\xi_{\text{auto}}$ , as a function of  $\Delta v = H\Delta r$ , at  $z = 2.4$ . The models are denoted as in Fig. 5

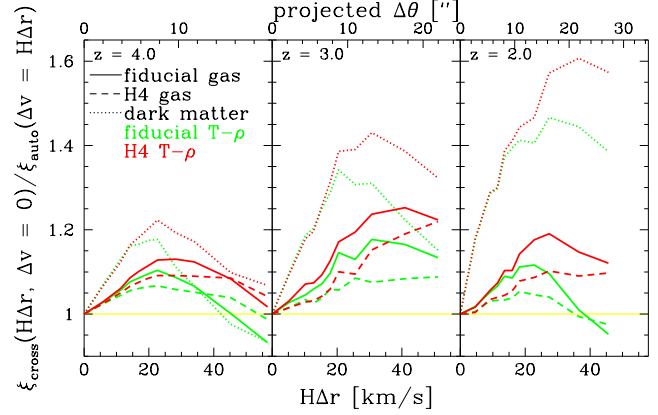


**Figure 8.** Normalized cross-correlation functions showing the anisotropy of the Ly $\alpha$  forest,  $\xi_{\text{cross}}/\xi_{\text{auto}}$ , as a function of  $\Delta v = H\Delta r$ , at  $z = 4, 3$ , and  $2$ . The models are denoted as in Fig. 5

In Paper I we showed that the flux decrement PDFs for each of these  $T$ - $\rho$  relations are fairly distinct, so some of the model differences in  $p(D_2 - D_1)$  could reflect differences in the underlying flux PDFs. We can remove this effect by converting from flux decrement  $D$  to pixel rank  $R \equiv p(< D)$ , the fraction of pixels with a flux decrement lower than  $D$ . Of course, a fully successful model should reproduce the observed PDF, but here we wish to focus on transverse coherence and, therefore, remove any differences in the PDF caused by different temperature-density relations. Figure 10 shows that spectra generated from the H4 gas have rank difference distributions more strongly peaked around  $R_2 - R_1 = 0$  than spectra from the lower pressure, fiducial gas spectra. Changing the imposed temperature-density relation has less effect on the distributions than changing the underlying gas distribution, implying that (as expected) pressure rather than thermal broadening accounts for the larger transverse coherence. In general, the larger coherence appears at all redshifts, but it weakens with increasing  $\Delta r$ . Non-thermally broadened spectra (not shown) have broader  $R_2 - R_1$  distributions, so thermal broadening does play some role in transverse coherence. As with previous statistics, however, the lower resolution spectra differ from the fiducial case by about as much as spectra generated from different imposed  $T$ - $\rho$  relations. Figure 11 presents the  $z = 2.4$  predictions in greater detail for the fiducial and H4 gas only, plotting five ranges of  $R_1$  and comparing  $\Delta v = 0$  to  $\Delta v \sim 20 \text{ km s}^{-1}$ . The models are most easily distinguished at small  $\Delta v$  and at small  $\Delta r$ .

In general, the slope of the temperature-density relation is much more difficult to observationally constrain than  $T_0$  because most methods for measuring the  $T$ - $\rho$  relation are sensitive to only a limited range of  $\tau_{\text{HI}}$  and hence  $1 + \delta$ . Because (up to saturation) we can limit ourselves to a particular range of optical depth and thus  $1 + \delta$  when using *conditional* rank distributions, it might be possible to use this technique to constrain the slope of the temperature-density relation. We cannot test this possibility using our current simulations because the fiducial and H4 temperature-density relations have similar slopes at all redshifts (see Table 1).

## 4 CONCLUSIONS

Recent efficient searches for binary quasars have yielded large samples of quasars with angular separations of  $\lesssim 10''$  (Hennawi et al. 2006, 2009). The closely paired Lyman- $\alpha$  forest sightlines from

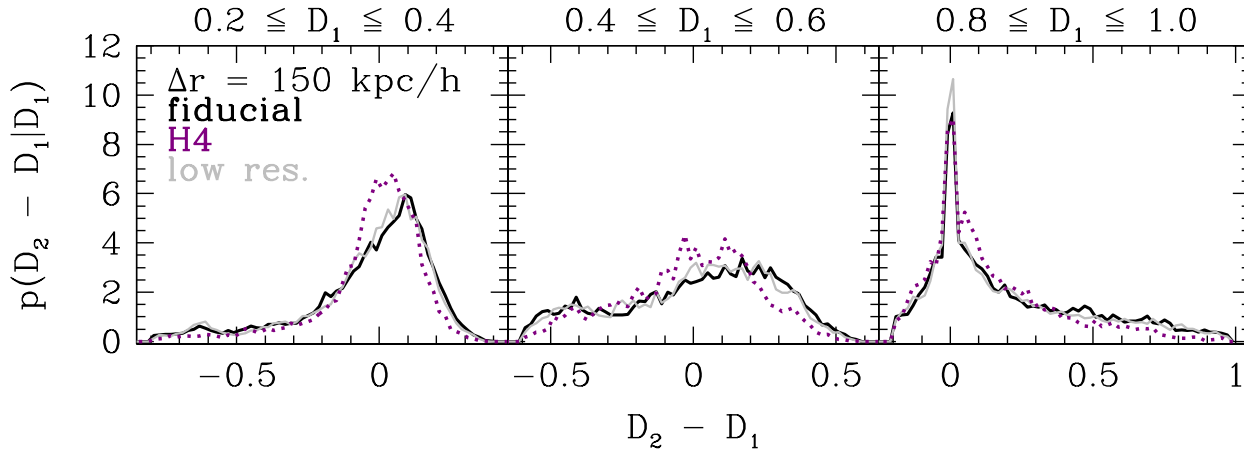


**Figure 9.** Flux decrement difference probability distributions,  $p(D_2 - D_1)$  v.  $(D_2 - D_1)$ , at  $z = 2.4$ , for  $\Delta v = 0$  and  $\Delta r = 150$ . The three columns show  $D_1 \in [0.2, 0.4]$  (left),  $D_1 \in [0.4, 0.6]$  (middle), and  $D_1 \in [0.8, 1.0]$  (right), with fiducial in black, H4 in purple (dotted), and the low resolution simulation in grey.

such quasar pairs are ideal for studying the small-scale transverse structure of the intergalactic medium. We have shown using a set of smoothed particle hydrodynamic simulations with different equations of state that the coherence of transverse structure at these scales is determined primarily by the level of pressure support, i.e. the Jeans length, of the absorbing gas and is relatively insensitive to the amount of thermal broadening along the line of sight. Given the surprisingly high temperatures implied by single-sightline analyses (see discussions in §1 and Paper I), it would be valuable to investigate the thermal state of the IGM by this largely independent method.

Flux correlation functions (measured by, e.g., Rollinde et al. 2003; Coppolani et al. 2006; D’Odorico et al. 2006; Marble et al. 2008a) and the two-point distributions of flux decrements or pixel ranks can all be used to distinguish among gas distributions with different temperatures like the fiducial and H4 models considered here. Because the redshift ranges and pair separations will be dictated by the specifics of the available data sample, we provide in the form of electronic tables our simulated spectra along paired lines of sight from the two simulations, which can be used to generate predictions tailored to a particular data sample. These samples of spectra are described in §2 and the caption to Table 1. We caution that the finite size of our simulation volume could cause statistical fluctuations and systematic effects on our predictions, especially at large  $\Delta r$  and  $\Delta v$ ; we will investigate this point in future work with larger simulations. The large increase in known quasar pairs, the ability of large telescopes to measure Lyman- $\alpha$  absorption spectra of relatively faint background sources, which have a high surface density on the sky, and the massive quasar sample expected from the Baryon Oscillation Spectroscopic Survey (Schlegel et al. 2009) will change the Ly $\alpha$  forest from a one-dimensional phenomenon to a three-dimensional phenomenon, opening new opportunities to constrain cosmology and the physics of the diffuse intergalactic medium.

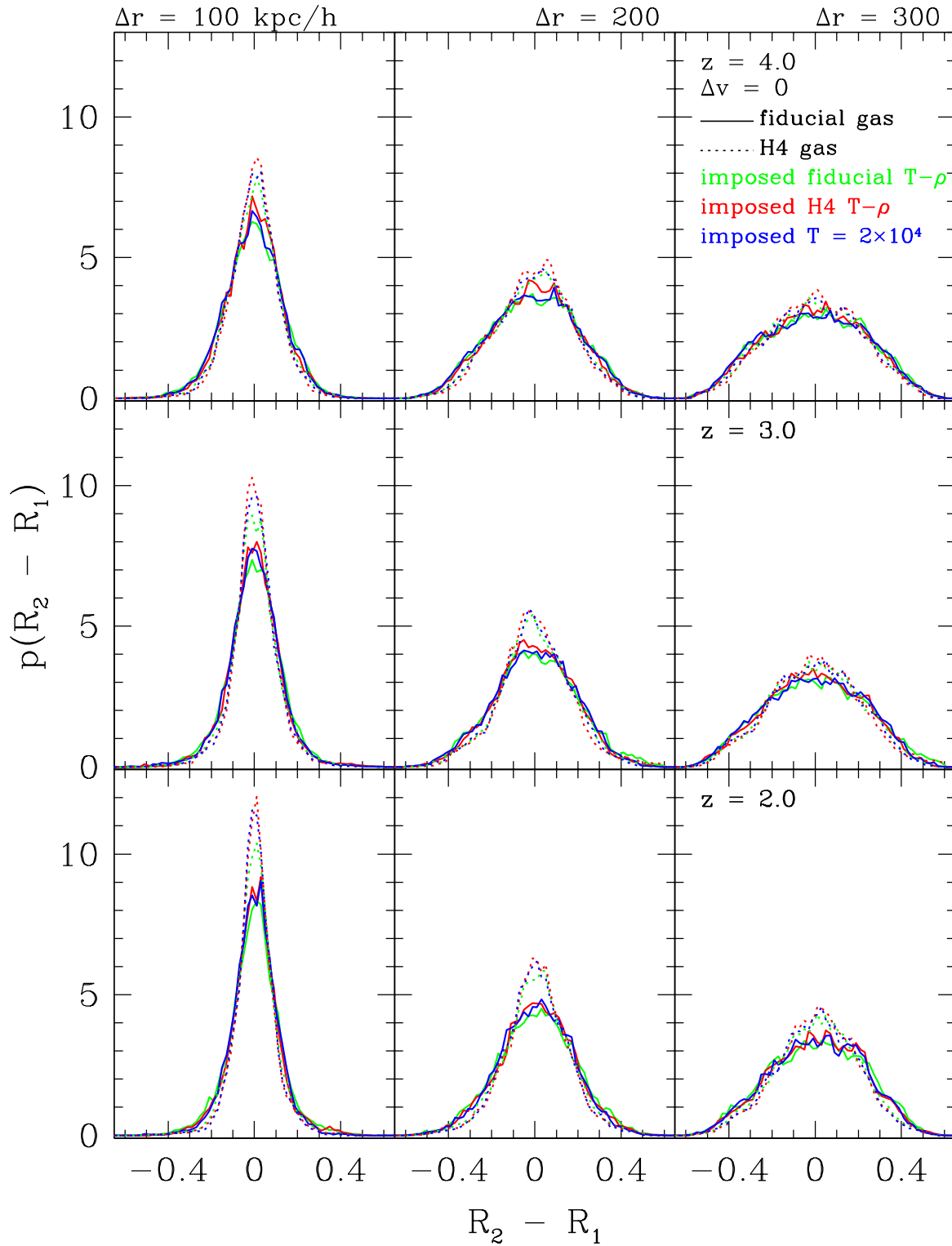
## ACKNOWLEDGMENTS

We acknowledge a seminar by Joe Hennawi at the Ohio State Center for Cosmology and Astro-Particle Physics, which inspired this

investigation; we also thank Joe Hennawi and Eduardo Rozo for helpful discussions and comments. We are grateful to the anonymous referee for thoughtful suggestions on the text. This work has been supported in part by NSF grant AST-0707985 and NASA ADP grant NNX08AJ44G.

## REFERENCES

- Alcock, C. & Paczynski, B. 1979, *Nature*, 281, 358
- Bechtold, J., Crofts, A. P. S., Duncan, R. C., & Fang, Y. 1994, *ApJL*, 437, L83
- Bi, H. & Davidsen, A. F. 1997, *ApJ*, 479, 523
- Bolton, J. S., Viel, M., Kim, T.-S., Haehnelt, M. G., & Carswell, R. F. 2008, *MNRAS*, 386, 1131
- Cen, R., Miralda-Escudé, J., Ostriker, J. P., & Rauch, M. 1994, *ApJL*, 437, L9
- Charlton, J. C., Anninos, P., Zhang, Y., & Norman, M. L. 1997, *ApJ*, 485, 26
- Coppolani, F., Petitjean, P., Stoehr, F., Rollinde, E., Pichon, C., Colombi, S., Haehnelt, M. G., Carswell, B., & Teyssier, R. 2006, *MNRAS*, 370, 1804
- Crofts, A. P. S. & Fang, Y. 1998, *ApJ*, 502, 16
- Desjacques, V. & Nusser, A. 2005, *MNRAS*, 361, 1257
- Dinshaw, N., Impey, C. D., Foltz, C. B., Weymann, R. J., & Chaffee, F. H. 1994, *ApJL*, 437, L87
- D’Odorico, V., Cristiani, S., D’Odorico, S., Fontana, A., Giallongo, E., & Shaver, P. 1998, *A&A*, 339, 678
- D’Odorico, V., Viel, M., Saitta, F., Cristiani, S., Bianchi, S., Boyle, B., Lopez, S., Maza, J., & Outram, P. 2006, *MNRAS*, 372, 1333
- Fang, Y., Duncan, R. C., Crofts, A. P. S., & Bechtold, J. 1996, *ApJ*, 462, 77
- Faucher-Giguère, C.-A., Prochaska, J. X., Lidz, A., Hernquist, L., & Zaldarriaga, M. 2008, *ApJ*, 681, 831
- Gnedin, N. Y. & Hui, L. 1998, *MNRAS*, 296, 44
- Hennawi, J. F., Myers, A. D., Shen, Y., Strauss, M. A., Djorgovski, S. G., Fan, X., Glikman, E., Mahabal, A., Martin, C. L., Richards, G. T., Schneider, D. P., & Shankar, F. 2009, *arXiv:0908.3907*





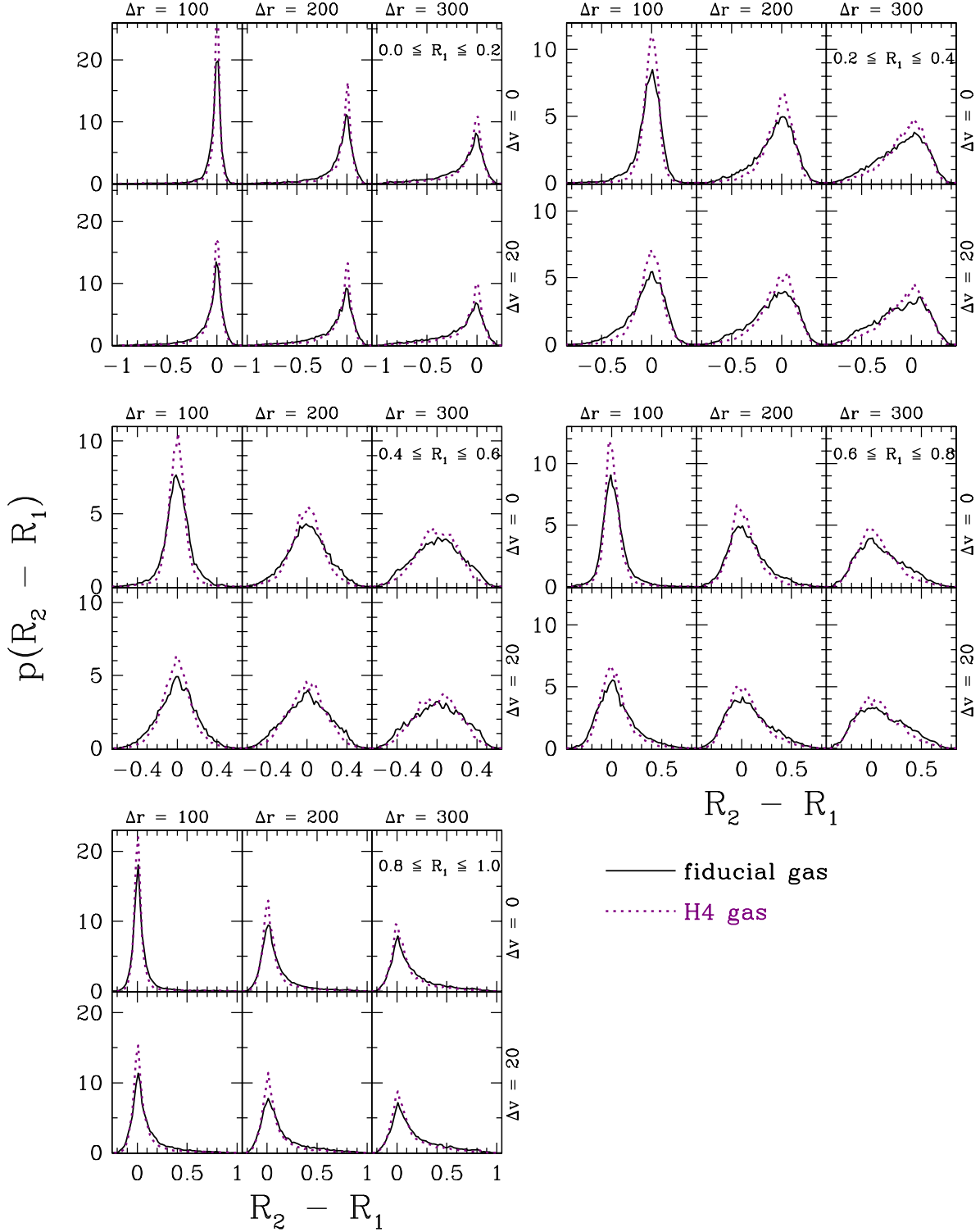


**Figure 11.** Probability distributions for differences in flux decrement rank,  $p(R_2 - R_1)$  v.  $(R_2 - R_1)$  for  $\Delta r = 100, 200$ , and  $300 h^{-1}$  kpc comoving and  $\Delta v = 0$  and  $20 \text{ km s}^{-1}$  as labelled, for a range of  $R_1$  at  $z = 2.4$ . The H4 gas (purple, dotted) is more strongly peaked around  $R_2 = R_1$  than the fiducial gas (black, solid) because the hotter gas has longer Jeans lengths and thus a higher transverse coherence.

Hennawi, J. F., Strauss, M. A., Oguri, M., Inada, N., Richards, G. T., Pindor, B., Schneider, D. P., Becker, R. H., Gregg, M. D., Hall, P. B., Johnston, D. E., Fan, X., Burles, S., Schlegel, D. J., Gunn, J. E., Lupton, R. H., Bahcall, N. A., Brunner, R. J., & Brinkmann, J. 2006, *AJ*, 131, 1

Hernquist, L., Katz, N., Weinberg, D. H., & Miralda-Escudé, J. 1996, *ApJL*, 457, L51+

Hinshaw, G., Weiland, J. L., Hill, R. S., Odegard, N., Larson, D., Bennett, C. L., Dunkley, J., Gold, B., Greason, M. R., Jarosik, N., Komatsu, E., Nolte, M. R., Page, L., Spergel, D. N., Wollack, E., Halpern, M., Kogut, A., Limon, M., Meyer, S. S., Tucker, G. S., & Wright, E. L. 2009, *ApJS*, 180, 225

Hui, L. & Gnedin, N. Y. 1997, *MNRAS*, 292, 27

Hui, L., Gnedin, N. Y., & Zhang, Y. 1997, *ApJ*, 486, 599

Hui, L., Stebbins, A., & Burles, S. 1999, *ApJL*, 511, L5

Katz, N., Weinberg, D. H., & Hernquist, L. 1996, *ApJS*, 105, 19

Marble, A. R., Eriksen, K. A., Impey, C. D., Bai, L., & Miller, L. 2008a, *ApJS*, 175, 29

Marble, A. R., Eriksen, K. A., Impey, C. D., Oppenheimer, B. D., & Davé, R. 2008b, *ApJ*, 675, 946

McDonald, P. & Miralda-Escudé, J. 1999, *ApJ*, 518, 24

McDonald, P., Miralda-Escudé, J., Rauch, M., Sargent, W. L. W., Barlow, T. A., & Cen, R. 2001, *ApJ*, 562, 52

McDonald, P., Miralda-Escudé, J., Rauch, M., Sargent, W. L. W., Barlow, T. A., Cen, R., & Ostriker, J. P. 2000, *ApJ*, 543, 1

Miralda-Escudé, J., Cen, R., Ostriker, J. P., & Rauch, M. 1996, *ApJ*, 471, 582

Miralda-Escudé, J., Rauch, M., Sargent, W. L. W., Barlow, T. A., Weinberg, D. H., Hernquist, L., Katz, N., Cen, R., & Ostriker, J. P. 1997, in *Structure and Evolution of the Intergalactic Medium from QSO Absorption Line System*, ed. P. Petitjean & S. Charlot, 155–+

Rauch, M. & Haehnelt, M. G. 1995, *MNRAS*, 275, L76

Reisenegger, A. & Miralda-Escudé, J. 1995, *ApJ*, 449, 476

Ricotti, M., Gnedin, N. Y., & Shull, J. M. 2000, *ApJ*, 534, 41

Rollinde, E., Petitjean, P., Pichon, C., Colombi, S., Aracil, B., D’Odorico, V., & Haehnelt, M. G. 2003, *MNRAS*, 341, 1279

Schaye, J. 2001, *ApJ*, 559, 507

Schaye, J., Theuns, T., Rauch, M., Efstathiou, G., & Sargent, W. L. W. 2000, *MNRAS*, 318, 817

Schlegel, D., White, M., & Eisenstein, D. 2009, in *Astronomy, Vol. 2010, AGB Stars and Related Phenomena*, 314–+

Schneider, P., Kochanek, C. S., & Wambsganss, J. 2006, *Gravitational Lensing: Strong, Weak and Micro (Gravitational Lensing: Strong, Weak and Micro: , Saas-Fee Advanced Courses, Volume 33. ISBN 978-3-540-30309-1. Springer-Verlag Berlin Heidelberg, 2006)*

Springel, V. 2005, *MNRAS*, 364, 1105

Theuns, T., Schaye, J., Zaroubi, S., Kim, T.-S., Tzanavaris, P., & Carswell, B. 2002, *ApJL*, 567, L103

Viel, M., Matarrese, S., Mo, H. J., Haehnelt, M. G., & Theuns, T. 2002, *MNRAS*, 329, 848

Zhang, Y., Anninos, P., & Norman, M. L. 1995, *ApJL*, 453, L57+

at  $z = 2, 2.4, 3$ , and  $4$ . We show in Table ?? a portion of the spectra from the fiducial simulation at  $z = 2$ .

## APPENDIX A: FORMAT OF ASSOCIATED ELECTRONIC TABLES

We provide in the form of electronic tables our simulated spectra, the H I optical depth as a function of velocity and transverse separation, along paired sightlines from the fiducial and H4 simulations

**Table A1.** Sample paired spectra for the fiducial simulation at  $z = 2$ . Each set of 1250 lines corresponds to an independent sightline and its pairs. This table is published in their entirety online; a portion is shown here for guidance regarding its form and content.

$\nu$ [km s <sup>-1</sup> ]	$\tau_{\text{H I}}$ at transverse separation $\Delta r$ in $h^{-1}$ kpc comoving										
	0	50	100	125	150	175	200	250	300	400	500
0.456435	0.0331219	0.0285025	0.0288973	0.0297425	0.0303896	0.0308683	0.0316429	0.0371795	0.0469323	0.0521755	0.0474118
1.3693	0.0314817	0.0274538	0.0280237	0.0289396	0.0296675	0.0302456	0.0311112	0.0367447	0.0462802	0.0511294	0.0459319
2.28217	0.0301246	0.0265771	0.0272563	0.0282159	0.0290117	0.0296889	0.0306551	0.0364166	0.0457752	0.0502636	0.0446447
3.19504	0.0290066	0.0258401	0.0265773	0.0275609	0.028416	0.0291931	0.0302679	0.0361835	0.0454074	0.0495666	0.0435458
4.1079	0.028088	0.0252151	0.0259722	0.0269665	0.0278759	0.0287538	0.0299433	0.0360341	0.0451657	0.049025	0.0426295
5.02077	0.0273332	0.0246789	0.0254291	0.026426	0.0273876	0.0283671	0.0296758	0.0359581	0.0450378	0.0486238	0.041889
5.93364	0.0267117	0.0242127	0.0249388	0.0259346	0.026948	0.0280296	0.0294603	0.0359456	0.0450103	0.0483473	0.0413157
6.8465	0.0261978	0.0238013	0.0244938	0.0254882	0.0265548	0.0277383	0.0292924	0.0359874	0.0450688	0.0481795	0.0408999
7.75937	0.0257704	0.0234329	0.0240884	0.0250838	0.0262058	0.0274906	0.0291683	0.0360749	0.0451985	0.0481045	0.0406308
8.67224	0.0254127	0.0230988	0.0237179	0.024719	0.025899	0.0272841	0.0290847	0.0361998	0.0453839	0.0481074	0.0404972
...	...	...	...	...	...	...	...	...	...	...	...
1139.71	0.0374395	0.0312689	0.031053	0.031642	0.0320651	0.0323369	0.032963	0.0384191	0.0487098	0.0548428	0.0509672
1140.63	0.0350917	0.0297604	0.0298985	0.0306379	0.0311856	0.0315631	0.0322576	0.0377333	0.0477398	0.0534111	0.0490887
0.456435	0.0097211	0.0087474	0.00850357	0.00869964	0.0087597	0.00884541	0.00929591	0.0102907	0.01099	0.0110082	0.00980152
1.3693	0.0102372	0.00920984	0.00901555	0.00928603	0.00938722	0.00950945	0.0100469	0.0111618	0.0118516	0.0117359	0.0103104
...	...	...	...	...	...	...	...	...	...	...	...

**Table A2.** Same as Table A1 but for the H4 simulation at  $z = 2$ .

$\nu$ [km s <sup>-1</sup> ]	$\tau_{\text{H I}}$ at transverse separation $\Delta r$ in $h^{-1}$ kpc comoving										
	0	50	100	125	150	175	200	250	300	400	500
0.456435	0.0748727	0.0594009	0.0534443	0.052653	0.0523501	0.0518654	0.0500443	0.0488191	0.050699	0.0684818	0.114494
1.3693	0.0724616	0.0568817	0.0510125	0.0501911	0.049856	0.0494814	0.0478177	0.0468376	0.0485793	0.0659898	0.111661
2.28217	0.070031	0.0544353	0.0486847	0.0478525	0.0475057	0.0472524	0.0457502	0.0450143	0.0466329	0.0637098	0.108938
...	...	...	...	...	...	...	...	...	...	...	...
1139.71	0.0795899	0.0646117	0.0585712	0.0578997	0.0577296	0.0570707	0.0549619	0.0532615	0.0554679	0.0741066	0.120519
1140.63	0.0772525	0.0619816	0.0559683	0.0552269	0.0549786	0.054398	0.0524273	0.0509605	0.0529949	0.0711876	0.117445
0.456435	0.0156331	0.0160474	0.0163963	0.0163615	0.0158782	0.015466	0.0152769	0.0141906	0.0136551	0.0121923	0.0112008
...	...	...	...	...	...	...	...	...	...	...	...

**Table A3.** Same as Table A1 but for the fiducial simulation at  $z = 2.4$ .

[illegible]

**Table A4.** Same as Table A1 but for the H4 simulation at  $z = 2.4$ .

[illegible]

**Table A5.** Same as Table A1 but for the fiducial simulation at  $z = 3$ .

[illegible]

**Table A6.** Same as Table A1 but for the H4 simulation at  $z = 3$ .

[illegible]

**Table A7.** Same as Table A1 but for the fiducial simulation at  $z = 4$ .

[illegible]

**Table A8.** Same as Table A1 but for the H4 simulation at  $z = 4$ .

[illegible]